Mixing in the stratified interface of the Faroe Bank Channel overflow: The role of transverse circulation and internal waves

Knut S. Seim[1] and Ilker Fer[2]

Received 12 November 2010; revised 19 April 2011; accepted 29 April 2011; published 27 July 2011.

[1] The overflow of cold water across the Faroe Bank Channel sill is a significant volume flux of dense water to the North Atlantic Ocean. Using observations of hydrography, current and microstructure from a 1 week cruise and 2 month long time series from moored instruments, we address the role of transverse circulation and internal waves in mixing in the stratified 100 m thick plume-ambient interface. The streamwise momentum budget is dominated by a balance between the pressure gradient and bottom friction; the entrainment stress is negligible. The transverse momentum budget is in geostrophic balance, and the transverse velocity variability is governed by the internal streamwise pressure gradient. The transverse geostrophic flow in the interfacial layer is opposed by the bottom Ekman transport. The shear associated with the interfacial jet lowers the Richardson number and enhances dissipation rates. Convective overturning events observed on the upslope side suggest a link between the transverse circulation and the vertical mixing on the upper slope. Several independent threads of evidence support the transverse circulation as an important mixing mechanism for the overflow plume. In the ambient, dissipation rates inferred from fine-scale shear and density profile measurements are in good agreement with direct measurements, supporting internal wave breaking as a dominant mechanism for dissipation of turbulent energy. In the interfacial layer, spectral distribution of internal wavefield is energetic. In addition to shear-induced mixing and entrainment in the interfacial layer, internal wave breaking is likely to be important for the dissipation of turbulent energy and should not be ignored.

Citation: Seim, K. S., and I. Fer (2011), Mixing in the stratified interface of the Faroe Bank Channel overflow: The role of transverse circulation and internal waves, *J. Geophys. Res.*, *116*, C07022, doi:10.1029/2010JC006805.

1. Introduction

[2] The southward export of cold, dense water from the Nordic Seas to the North Atlantic across the Greenland-Scotland ridge and the associated water mass transformation are an important part of the Atlantic Meridional Overturning Circulation. About one third of this export is through the Faroe Bank Channel (FBC, Figure 1), the deepest passage from the Nordic Seas, in form of a bottom-attached dense plume (overflow hereafter) [*Hansen and Østerhus*, 2007]. Under the influence of pressure gradient, bottom friction, and the Earth's rotation, the overflow descends the Iceland-Faroe slope and mixes with overlaying water [*Saunders*, 2001; *Mauritzen et al.*, 2005; *Fer et al.*, 2010b]. The FBC region is one of the most studied overflow regions and has been the main focus of several projects and field studies, see *Borenäs and Lundberg* [1988], *Hansen and Østerhus* [2000], *Saunders* [2001], *Borenäs and Lundberg* [2004], and *Hansen and Østerhus* [2007] for detailed reviews of the FBC overflow. Since 1995, the overflow has been monitored by moorings at the sill crest [*Hansen and Østerhus*, 2007]. Here we concentrate on one prominent feature that influences the dynamics and mixing of the overflow plume: the thick stratified interfacial layer.

[3] Using recent observations which form a subset of the data presented in this paper, *Fer et al.* [2010b] report the following salient features of the plume, including its vertical and turbulence structure: (1) the overflow plume has a typical speed of 0.5–1 m s^{-1}, reaching a maximum of 1.35 m s^{-1} as it exits the FBC and enters the Iceland-Faroe Slope; (2) in the vertical a well-mixed, 70 ± 35 m thick, bottom layer (BL) is separated from the overlaying water by a 120 ± 60 m thick interfacial layer (IL), and (3) the dissipation rate of turbulent kinetic energy, ε, is enhanced in the bottom boundary layer and IL, but is significantly less in the well-mixed core of the plume, away from the bottom boundary layer. Here we hypothesize that the presence of a thick IL has significant consequences for the dynamics of the overflow, particularly for the mixing with the overlaying water.

[1]Department of Marine Technology, Norwegian University of Science and Technology, Trondheim, Norway.
[2]Geophysical Institute, University of Bergen, Bergen, Norway.

0148-0227/11/2010JC006805

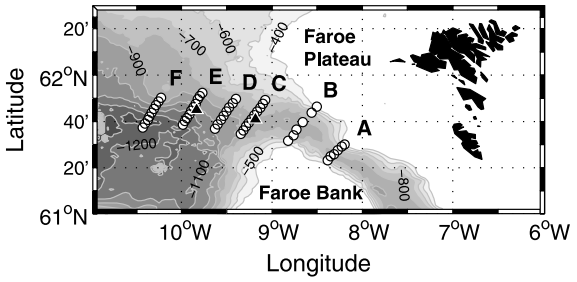

Figure 1. Map of all stations (circles) occupied during the June 2008 survey. The positions of the two moorings used in this study (CM and EM) are marked with triangles.

Thick and stratified interfacial layers have previously been observed in other major overflows [*Peters and Johns*, 2005; *Girton and Sanford*, 2003; *Price et al.*, 1993].

[4] *Seim et al.* [2010], comparing results from a regional simulation of the FBC overflow with the observations of *Fer et al.* [2010b], have pointed at the inadequacy of state-of-the-art turbulence closures in representing the mixing in the IL; model dissipation rates were up to 2 orders of magnitude less than the observations. The authors link the underestimated mixing in the IL to unresolved processes, such as transport of turbulent kinetic energy (TKE) [*Umlauf*, 2009], mixing due to breaking internal waves [*D'Asaro and Lien*, 2000], and the lack of sources of mixing for Richardson numbers (Ri) above a finite threshold set in turbulence closures. In most overflows intense mixing occurs at localized regions where low gradient Richardson numbers and large bulk Froude numbers (Fr) are colocated, suggesting that the TKE source for vertical mixing is the kinetic energy of the mean flow [*Baringer and Price*, 1997]. In the case of the FBC overflow this happens between 50 and 100 km downstream of the sill; turbulence, however, is energetic along the path of the plume despite low Fr and Ri in the order of unity. Data from various sources [see, e.g., *Canuto et al.*, 2008] including our own measurements show evidence for significant mixing, although $Ri > 0.25$. According to *Baumert and Peters* [2009], the internal wave-turbulence transition will coexist with the shear instability and contribute to mixing for $0.25 < Ri < 0.5$. Recent models are developed which do not impose a finite critical Ri [*Canuto et al.*, 2008; *Umlauf*, 2009].

[5] The FBC overflow in the sill region is constrained by the narrow and shallow channel where the dense plume is in contact with both sidewalls. The overflow resembles a channelized, rotating gravity current. Downstream of the sill the channel widens and the overflow plume flows on open slope. In the vicinity of the sill, sections of density distribution of the overflow show pinching of the isopycnals at the Faroe Bank side (southwest wall) and their spread toward the northeast wall of the channel [*Borenäs and Lundberg*, 1988; *Saunders*, 1990; *Borenäs and Lundberg*, 2004; *Mauritzen et al.*, 2005]. This is proposed to be explained by a secondary cross-channel (transverse) circulation, first observed in expendable current profiler drops at the FBC sill [*Johnson and Sanford*, 1992]. In this paper we will use the term "secondary circulation" to refer to the cross-channel, transverse circulation. The large stress at the bottom causes a significant southwest, cross-stream Ekman flow in the frictional bottom boundary layer (BBL) opposed by a northeast flow of similar magnitude in the IL. Note that BBL is different than and can be shallower than the well-mixed BL. This secondary circulation with opposite flows at the top and bottom of the overflow suggests a spiral character in the overflow leading to considerable mixing and warming [*Johnson and Sanford*, 1992]. The spiral character of a dense overflow confined in a channel has later been confirmed in laboratory experiments [*Johnson and Ohlsen*, 1994; *Darelius*, 2008]. The importance of the bottom friction for the downward steering of dense water, so-called "frictional control", has been emphasized in theoretical work on rotating bottom gravity currents [*Wåhlin*, 2002, 2004; *Darelius and Wåhlin*, 2007; *Umlauf and Arneborg*, 2009b]. The frictional control is a mechanism, independent of any transverse stratification or secondary circulation, whereby the down-channel velocity is adjusted exactly such that friction balances the down-channel pressure gradient, and the cross-channel Ekman transport is compensated by the oppositely directed geostrophic transport due to the down-channel tilt of the interface [*Wåhlin*, 2002, 2004; *Umlauf and Arneborg*, 2009b]. Analyzing data from a channelized, shallow rotating gravity current in the western Baltic Sea, *Umlauf and Arneborg* [2009a, 2009b] find the mechanism of "frictional control" to be supported by their measurements. A nearly geostrophically balanced jet in the interface, transporting interfacial fluid to the right of the down-channel flow, is found to have important implications for the development of the density field and the entrainment process. Further investigation of this shallow gravity current with a series of idealized numerical experiments show that the secondary circulation laterally advects the entrained ambient water and ultimately mixes in the bottom layer on the opposite side of the channel [*Umlauf et al.*, 2010]. This shallow gravity current is characterized by Ekman numbers in the order of unity and subcritical Froude numbers, fundamentally different from the deep FBC overflow with Ekman numbers one order of magnitude smaller.

[6] On the open slope where the plume is not constrained by channel walls, whether a secondary circulation can be maintained is uncertain. The observations presented in this study show a pronounced transverse circulation downstream of the sill. Similar dynamics has been observed in the well-mixed BL of the North Atlantic deep western boundary current [*Stahr and Sanford*, 1999]. In this paper, we describe the secondary circulation in the deep FBC overflow and discuss its role in mixing.

[7] In this study we use a data set from a survey of the FBC overflow conducted in June 2008, including hydrography, current and turbulence measurements, and 2 month long time series from moored instruments to study the processes at the thick IL, with focus on the secondary circulation and role of internal waves in mixing of the plume. The measurements, sampling and processing details are described in section 2. We present and discuss the dynamics of the secondary circulation, its cross-slope structure and its role in mixing in section 3. Subsequently, the internal wave energy in the interfacial layer and the wave dissipation in the

Table 1. Details for the Moorings CM and EM[a]

Parameter	CM	EM
Lon/Lat	9°11′W/61°41′N	9°50′W/61°45′N
Depth	804 m	990 m
In/out	14.05/18.07.2008	14.05/17.07.2008
P	210, 150 m	100, 70, 50 m
T	210, 201 m	160, 100 m
	200-140, 10 m interval	98, 70 m
	148, 101, 20 m	60, 50, 20 m
C	201, 150, 101, 20 m	100, 70, 60 m
u/*v*	210-110, 2 m interval (ADCP)	150-50, 2 m interval (ADCP)
	100, 20 m (RCM7)	160, 20 m (RCM7)

[a]The instrument sensor positions are given as height above bottom.

ambient and in the interfacial layer are discussed (section 4). Conclusions are drawn in section 5.

2. Measurements

2.1. Sampling

[8] Measurements were made during the cruise of R.V. Håkon Mosby between 29 May and 8 June 2008, and as time series from moored instruments deployed in the period 14 May to 18 July 2008. The data set obtained during the cruise includes vertical properties of hydrography and velocity from 63 casts with a conductivity-temperature-depth (CTD, Sea-Bird Electronics SBE911+) package equipped with a pair of down- and up-looking lowered acoustic Doppler current profilers (LADCP's, RD-Instruments 300 kHz Workhorse), and of turbulence profiles from 90 casts with a vertical microstructure profiler (VMP, Rockland Scientific Instruments). The VMP can profile down to 2000 m and is equipped with accurate pumped SBE-CTD sensors, a pair of airfoil shear probes used for measuring the dissipation rate of turbulent kinetic energy (ε), and fast response temperature and conductivity sensors. The turbulence and slow sensors sampled at 512 Hz and 64 Hz, respectively, at a nominal profiling speed of 0.6 m s^{-1}. Stations were taken at six cross sections along the path of the overflow plume starting from the sill crest (section A) to about 120 km downstream of the sill (section F, Figure 1), and at two stations, about 12 h long each, with repeated VMP/CTD/LADCP colocated with the moorings. Two moorings, CM and EM, are positioned approximately in the center of section C and section E respectively, about 60 km and 100 km downstream of the sill, recording for 2 months duration. The instrument details of the moorings are given in Table 1. The CM mooring was equipped with two Aanderaa RCM7 currentmeters at 20 and 100 m height above bottom (HAB), one downward looking ADCP (RDI 300 kHz Workhorse) at 200 m HAB and a number of temperature (SBE39 and RBR TR-1050) and CTD (SBE37 MicroCAT) loggers at different levels. The EM mooring had a similar setup, but with an upward looking ADCP (RDI 300 kHz Workhorse) at 50 m HAB and RCM7 currentmeters at 20 and 160 m HAB (see Table 1). The sampling rate was 1 min for SBE and RBR, 5 min for ADCPs and 10 min for RCM7s. The ADCPs pinged every 6 s, averaged ensembles of 50 profiles, and profiled at 2 m vertical depth bins.

2.2. Processing Details and Layer Definitions

[9] The velocity profiles from the LADCP are calculated as 4 m vertical averages using the inverse method [*Visbeck*, 2002] constrained by accurate shipboard navigation and bottom tracking by the LADCP. In order to obtain as synoptic as possible section property distributions, velocity profiles are detided using a barotropic tidal model [*Egbert et al.*, 1994] for the European Shelf at 1/30° resolution. Tidal velocity is within 3 to 34% (18% on the average) of the maximum velocity at a given station [*Fer et al.*, 2010b]. Neither the estimates of stress nor the shear vertical wave number spectra shown later are influenced by detiding. The profiles of ε are obtained from the shear probes of VMP as 1 m vertical averages, by integrating the vertical wave number spectrum of shear and assuming isotropy. The noise level in ε measurements based on shear probe data in quiet sections of the water column was 10^{-10} W kg^{-1}.

[10] We adopt right-handed Cartesian coordinates with positive x, y and z directed toward upstream (hence the streamwise, downstream component is $-u$), to the right looking downstream, and up, respectively. The velocity profiles inferred from LADCP are rotated into streamwise ($-u$) and transverse (v) components with respect to the direction of the maximum velocity in the bottom 200 m. The depth of the plume interface, z_i, and the plume thickness are inferred from the σ_θ = 27.65 kg m^{-3} isopycnal [*Mauritzen et al.*, 2005]. The well-mixed BL thickness is estimated as the height above bottom where the density difference from the bottommost value exceeds 0.01 kg m^{-3}. The stratified IL is defined as the layer between the top of BL and the depth above the interface where $\partial\sigma_\theta/\partial z$ first drops below 5×10^{-4} kg m^{-4}. These layer definitions follow *Fer et al.* [2010b] and were found to delineate BL and IL robustly. The thickness of BL (70 ± 35 m) is comparable to the level of the near-bottom velocity maximum (71 ± 50 m). The height of shear maximum above the velocity maximum

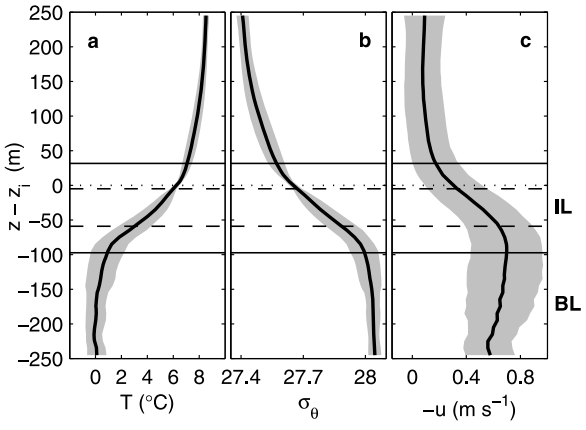

Figure 2. Survey-averaged profiles of (a) temperature, T, (b) potential density anomaly, σ_θ, and (c) streamwise velocity, $-u$, for all stations sampling the overflow. The solid lines mark the top of the interfacial layer (IL) and top of the well-mixed bottom layer (BL), the dashed lines are the 3°C and 6°C isotherms, and the dotted line is the plume interface z_i. Vertical axis is depth relative to z_i. Individual profiles are averaged in bins of $z - z_i$ = 10 m. Grey envelopes are ±1 standard deviation.

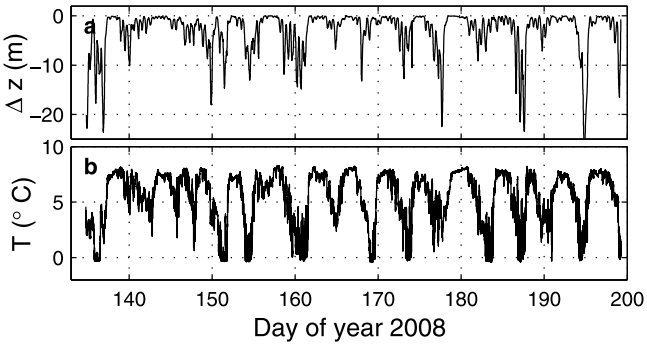

Figure 3. (a) Variability of vertical displacement of the microcat at 150 m HAB at mooring CM calculated from the measured pressure and (b) temperature recorded by the same instrument.

is 132 ± 66 m HAB, below the top of the plume (190 ± 75 m HAB) detected by the density gradient threshold.

[11] Survey-averaged profiles of temperature, density and the streamwise velocity are shown in Figure 2 which also identifies the mean positions of BL and IL. Constructing average profiles from a bottom plume in highly variable water depth is not trivial, and distortions in averages will occur depending on the reference level chosen for the z coordinate. Because the focus of this paper is in IL, we reference the vertical axis to the plume interface, z_i. Deeper parts of the average profiles are distorted by the choice of reference level and are not representative of the near-bottom structure. Average profiles with respect to HAB can be seen in the work of *Fer et al.* [2010b]. The survey averaged profiles are representative of the general structure of the overflow plume, but not of individual sections or stations due to the high temporal and spatial variability.

[12] The velocity profiles from the moored instruments are projected into the streamwise and transverse components, relative to the direction of the maximum velocity in the time-averaged velocity profile of each mooring. The compass error associated with the ADCPs is ±5°. The direction of the velocity maximum of individual hourly profiles is variable, but agrees to within ±15° of that inferred from the time-averaged profile, hence the direction of the overflow plume velocity maximum is stable. The projection of the velocity components is a major source of error and is discussed in section 3.1. Due to the limited vertical coverage of the moorings, IL cannot be resolved. In the following, when discussing the properties and circulation in IL inferred from the mooring data, we use the layer between 3 and 6°C isotherms. This is representative of the IL, but covers about half the IL thickness (Figure 2).

2.3. Mooring Motion

[13] Due to strong and highly variable currents, the moored instruments are regularly displaced from their target depth with maximum vertical displacements of about 20 m (Figure 3a). In Figure 3 the covariability of the vertical displacement with the passage of cold pulses of overflow is illustrated by showing the vertical displacement together with the temperature measured at 150 m HAB at the CM mooring. This instrument nominally located at 150 m HAB is in the IL (see Figure 10a). The instrument is knocked down into the BL from its nominal position in the IL when strong negative displacement occurs. The periodicity of the signal suggests that the low temperature incidents, and negative displacement due to strong currents, are associated with the mesoscale variability apparent in both measurements [*Seim et al.*, 2010; *Mauritzen et al.*, 2005; *Geyer et al.*, 2006] and numerical simulations [*Seim et al.*, 2010; *Riemenschneider and Legg*, 2007; *Ezer*, 2006]. The influence of mooring motion on vertical displacement calculations are discussed in section 4.2. The mesoscale variability apparent in the present data set is the topic for an ongoing study and will not be addressed here.

3. Secondary Circulation

3.1. Dynamics

[14] *Johnson and Sanford* [1992] attributed the pinching of the isotherms in the FBC overflow at the sill to a transverse, secondary circulation in the overflow. The large bottom stress exerted on the overflow gives rise to a cross-flow transport of about 1/16 of the overflow transport in the bottom layer (bottom Ekman transport) and a transport of similar magnitude in the opposite direction in the interfacial layer associated with strong shear and mixing (interfacial Ekman transport) [*Johnson and Sanford*, 1992]. We will show that on the open slope farther downstream a similar secondary circulation exists, however, the dynamics is different: the interfacial Ekman transport is not significant in driving the secondary circulation, but the geostrophically balanced part of the transport in IL plays a key role.

[15] Later studies of dense water flow in channels link the cross-channel flow in the interfacial layer to the along-channel tilt of isopycnals [*Wåhlin*, 2004; *Umlauf and Arneborg*, 2009b] resulting in a transverse geostrophic flow. Such an idealized geostrophically balanced dense water flow and its structure, adopted for an open slope, are illustrated in Figure 4. In these simplified models the flow is stationary and the interfacial slope coincide with the bottom slope. Downstream of the FBC sill crest, the dense plume flows along the Iceland-Faroe slope and is no longer a channel flow; we use streamwise and transverse directions in analogy with down-channel and cross-channel directions. Following *Umlauf and Arneborg* [2009b], we assume stationary flow, negligible horizontal mixing and negligible advection except for advection of the streamwise momentum to obtain the shallow water equations:

$$\frac{\partial u^2}{\partial x} + \frac{\partial uw}{\partial z} - fv = \int_z^\infty \frac{\partial b}{\partial x}\, d\hat{z} - \frac{1}{\rho_0}\frac{\partial \tau_x}{\partial z}, \tag{1a}$$

$$fu = \int_z^\infty \frac{\partial b}{\partial y}\, d\hat{z} - \frac{1}{\rho_0}\frac{\partial \tau_y}{\partial z}, \tag{1b}$$

where f is the Coriolis parameter, τ_x and τ_y denote the horizontal components of the vertical flux of momentum, and b is the buoyancy with respect to the background density, ρ_0:

$$b = -g\frac{\rho - \rho_0}{\rho_0}.$$

Here ρ and g denote the density and the acceleration of gravity. Different from *Umlauf and Arneborg* [2009b], who

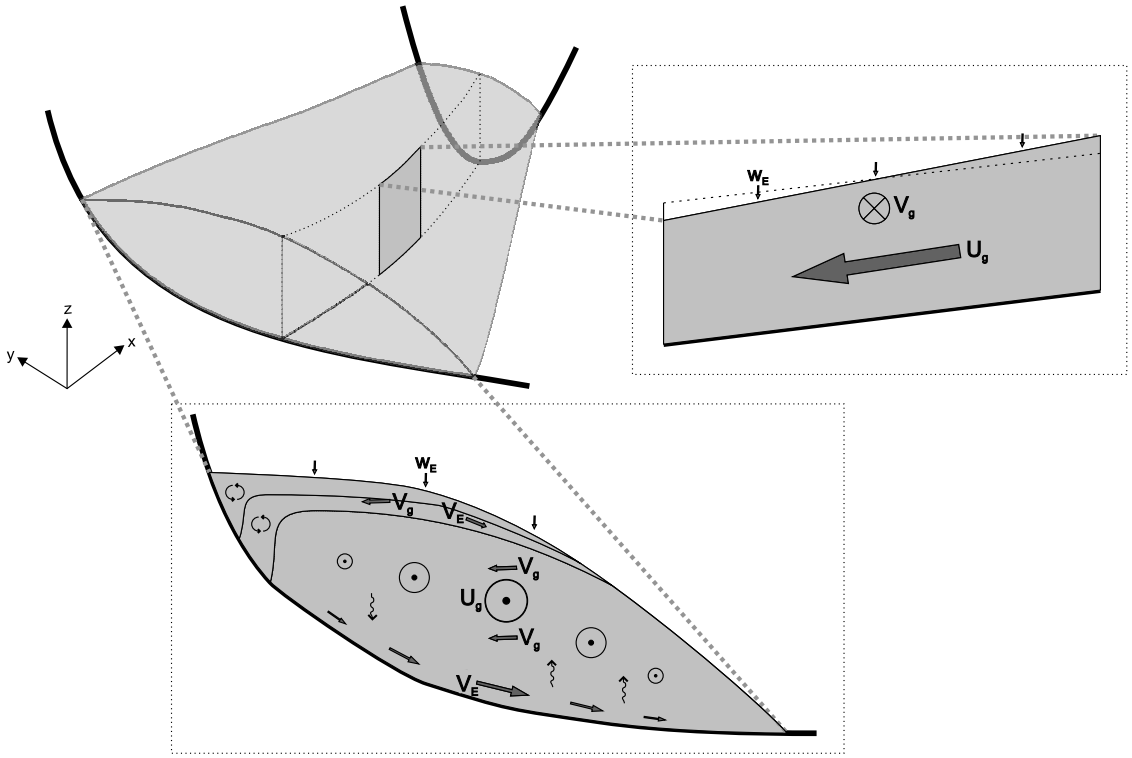

Figure 4. Illustration of the FBC overflow plume structure and the secondary circulation.

assumed identical streamwise slope of bottom and interface, we retain variable streamwise interface slope, i.e., *Umlauf and Arneborg* [2009b] approximate the pressure gradient in equation (1a) by $-bS_x$, where S_x is the along-channel bottom slope.

[16] The mean profiles of streamwise and transverse velocity components, temperature, T, and buoyancy frequency, N, inferred from the mooring data at CM 60 km downstream of the sill are shown in Figure 5. Also shown are the profiles averaged over 7 CTD-LADCP casts within 8 km of the mooring position, collected during the June 2008 cruise. All averages are with respect to HAB and should not be compared to Figure 2. The comparison suggests that, although limited by the short duration of the cruise, survey-mean profiles (see Figure 2) which includes 63 CTD-LADCP profiles in contrast to only 7 included in Figure 5, will be representative of time-mean properties averaged over the mesoscale variability not resolved by the cruise data. The velocity profiles from the mooring CM (Figure 5a) clearly show the signature of the secondary circulation: a weak flow of about 100 m thick, stratified IL to the right of streamwise velocity opposed by a return current at 20 m HAB, consistent with the Ekman flow in the frictional boundary layer. There are only two current meter levels in the bottom 100 m, and the time-mean vertical structure close to the bottom is not resolved. Mean profiles from the LADCP supplement the mooring data and support opposing transverse flows in BBL and IL. The large discrepancy between the mooring-derived and LADCP-derived transverse velocity can be mainly attributed to sensitivity to the projection angle for rotation of the velocity components, however, the mesoscale variability also plays a role. The results presented in this study also show that the assumptions of stationarity and identical bottom/interfacial slopes will fail in the case of the FBC overflow.

[17] In Figure 6, the time evolution of the streamwise slope of the interfacial layer, estimated from the mean slope of the 3 and 6°C isotherms between moorings CM and EM, is shown together with the measured transverse and streamwise velocity averaged in the layer between the two isotherms. The slope of IL, and correspondingly the transverse geostrophic velocity, is highly variable in time, and the magnitude of the variability of the slope of IL is comparable to the streamwise bottom slope. The temporal variability occasionally leads to a negative slope of IL and a corresponding negative transverse velocity. The strong variability in the transverse velocity is linked to the mesoscale variability in the overflow streamwise velocity (Figure 6c) and thickness discussed by *Seim et al.* [2010]. In this region, the temperature-salinity relation is tight, and isotherms are representative of isopycnals. When inferred from a third degree polynomial fitted to temperature, we find density to be accurate to within an r.m.s. error of 0.01 kg m^{-3}. Within this layer, using density from T, we compute the geostrophic transverse velocity by integrating the thermal wind shear:

$$v_g = \frac{1}{f}\int_{z_{iso3}}^{z} \frac{\partial \overline{b}}{\partial x}\, d\hat{z}, \tag{2}$$

where v_g is referenced to the measured transverse velocity at $z = z_{iso3}$ and $\overline{b}$ is the 48 hour low-pass filtered buoyancy. The resulting geostrophic velocity has two contributions: due to the tilt of the isotherms parallel to

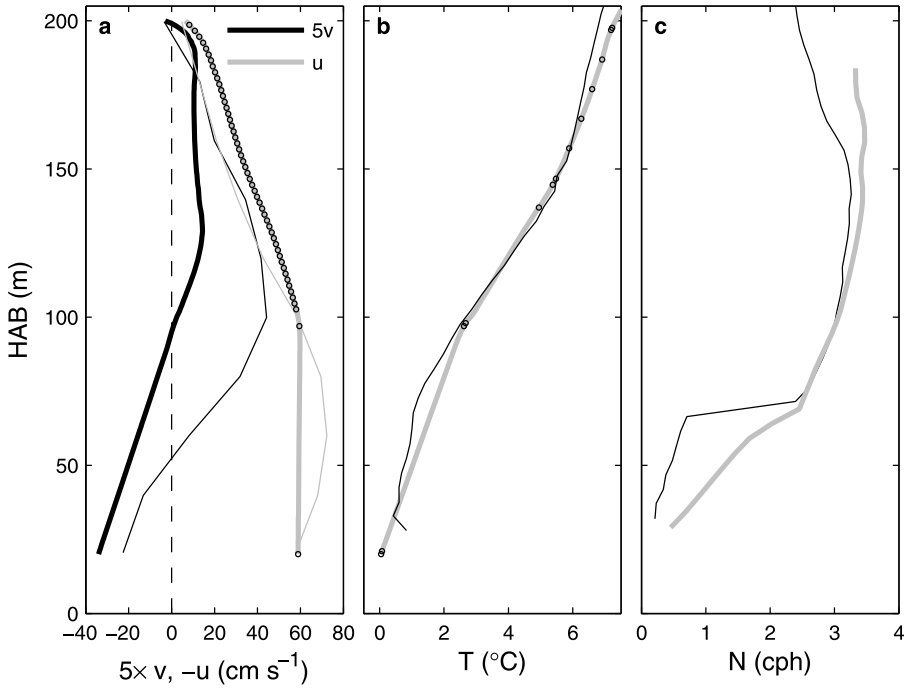

Figure 5. Mean profiles, averaged with respect to height above bottom (HAB), of (a) streamwise velocity, $-u$, and transverse velocity, v, multiplied by 5 for clarity, (b) temperature, and (c) buoyancy frequency, N inferred from CM mooring data. Thin lines show the profiles averaged using nearby 7 CTD-LADCP casts. Circles mark the time mean position where moored measurements are available.

the streamwise bottom slope (the assumption made by *Wåhlin* [2004] and *Umlauf and Arneborg* [2009b]) with little variation in time, and a highly variable component due to the "internal" pressure gradient resulting from the tilt of the isotherms relative to the bottom slope (Figure 7). The measured transverse velocity oscillates with the tilt of the isotherms with peak values exceeding 30 cm s^{-1} to the right (and 20 cm s^{-1} to the left) of the streamwise flow. The mean transverse velocity is 4 cm s^{-1} directed to the right of the streamwise velocity. The geostrophic velocity in the layer, v_g, is significantly larger than the observed transverse velocity. On the average v_g = 16 cm s^{-1}, with a contribution from the isotherms parallel to the streamwise bottom slope ("external" pressure gradient) of 14 cm s^{-1}. The contribution from the external pressure gradient is approximately constant in time and thus v_g attains significantly larger values due to the mesoscale variability.

[18] The projection of the measured velocity components into streamwise and transverse components leads to errors, both due to the choice of projection angle and also due to the compass measurement error. We define the streamwise direction as the direction of the velocity maximum of the time-averaged velocity profile from each mooring. When the above calculation is repeated using a projection relative to the direction of velocity maximum from hourly profiles at each mooring, the overall result is the same: in the interfacial layer v_g is larger than the measured transverse velocity. As a result of this calculation, average v_g = 12 cm s^{-1}, and the time-averaged transverse velocity is approximately zero. Further imposing a ±5° error on the streamwise direction and repeating the calculations leads to a velocity error of about 4 cm s^{-1} in v, on the average.

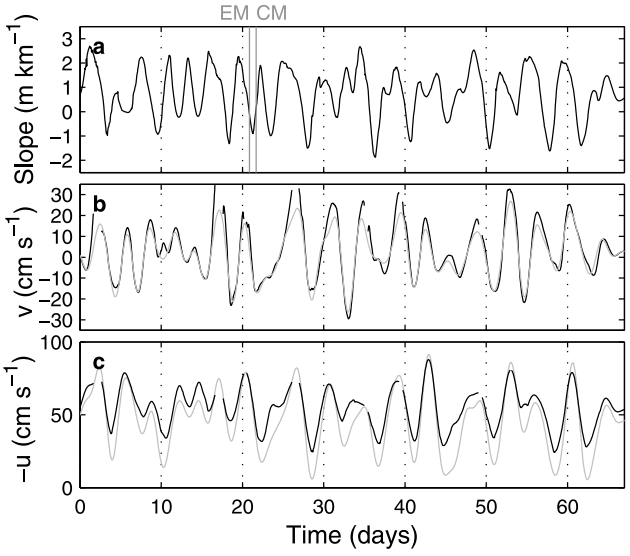

Figure 6. Time evolution of (a) the mean streamwise slope of the 3 and 6°C isotherms between moorings CM and EM, mean (b) averaged transverse and (c) streamwise velocity between the two moorings, and averaged between 3 and 6°C isotherms (black) and from the 3°C isotherm to the upper extent of the ADCP range (grey). Vertical lines in Figure 6a mark the start time of time series stations at EM and CM.

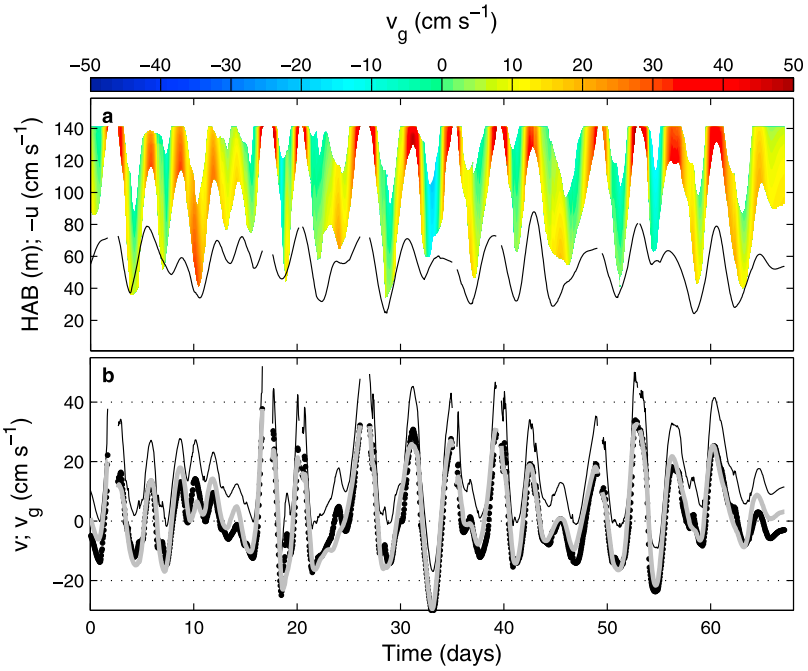

Figure 7. Time evolution of (a) vertical distribution of the geostrophically balanced transverse velocity v_g (color) together with the streamwise velocity $-u$ (black) averaged over the layer between 3 and 6°C isotherms, and (b) vertical mean of v_g calculated from the slope of isotherms between moorings CM and EM (black), the measured average transverse velocity, v (grey) and v_g with the contribution from the bottom slope removed (dotted).

[19] The difference between the measured transverse velocity and v_g is suggestive of an ageostrophic component in the interface that opposes v_g. Turbulent mixing and the entrainment stress in the interfacial layer will result in a transverse Ekman transport due to the streamwise flow. This ageostrophic transport in the interface opposes v_g. Relatively large velocity error estimated above hinders a firm conclusion on the role of the entrainment stress. We can state, however, that the ageostrophic transverse velocity due to interfacial stress is of comparable magnitude to the transverse geostrophic flow resulting from the external pressure gradient (Figure 7). The transverse velocity variability is thus governed by the tilt of the isotherms deviating from the bottom slope (i.e., the internal pressure gradient). A regression of v_g against v shows that the geostrophic component explains 80% of the variability in measured transverse velocity (85% when projected using the streamwise direction from hourly velocity profiles).

3.2. Cross-Slope Structure on the Slope

[20] *Stahr and Sanford* [1999] present a 2-D conceptual model of flow within the BBL and BL to explain their observations of the deep western boundary current at the Blake Outer Ridge. They observed a cross-slope asymmetry in the structure of the boundary layers and the along-slope velocity, the latter causing a cross-slope divergence of the bottom Ekman layer transport advecting light water downslope. This process, possibly also together with convection, leads to a thickening of the BL. The mean upwelling from the convergence drives a weak flow into the BL, which keeps density uniform throughout the BL (Figure 4). The cross-slope dynamical structure presented by *Stahr and Sanford* [1999] seems to offer a plausible explanation of the cross-stream structure of the secondary circulation of the FBC overflow (Figure 8) downstream of the sill on the Iceland-Faroe slope.

[21] In Figure 8b LADCP/CTD observations along section C show that the downslope (to the left of the streamwise flow) transverse velocity in the BL is opposed by a transverse flow in the IL. The maximum BL transverse velocity along the section is also associated with the maximum in the streamwise velocity. A successive convergence in the transverse velocity is expected together with a thickening of the well-mixed layer (BL, congruent to the bottom mixed layer in the work of *Stahr and Sanford* [1999]). Here the location of thickening of the BL coincides with the velocity maximum but is not downslope of the maximum as anticipated from the conceptual model. We attribute this discrepancy to the mesoscale variability of the overflow; occupation of the section, about 10 hours, will be influenced by this variability. The core of the dense overflow plume, associated with the largest buoyancy anomaly (Figure 8d), is located in the vicinity of the velocity maximum. As the secondary circulation transports this dense water upslope along isopycnals in the IL, it stratifies the interface and suppresses the vertical movement and thus thickening of the plume. Farther upslope, convective mixing, induced by relatively light interface water brought under the plume by bottom Ekman transport, will tend to thicken the plume. While this is not observed at the upslope stations at section C (Figure 8a), the mooring data reveal the presence of convective overturning and well-mixed layers on the slope (section 3.4).

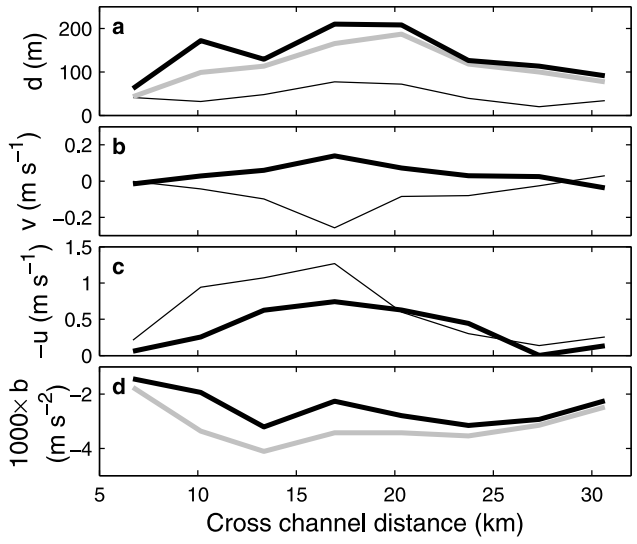

Figure 8. Distribution of (a) top of BL (thin), plume interface (grey), and top of IL (thick black), (b) average transverse velocity, v, and (c) average streamwise velocity, $-u$, in BL (thin) and IL (thick), and (d) buoyancy, b, averaged over the plume thickness (defined by the plume interface, grey) and over IL (black) along section C. Distance is relative to the deepest station on the Faroe-Island Slope; no plume water was detected in the first two stations. The Faroe Bank is on the left and the Faroe Plateau is on the right.

3.3. Bottom Versus Entrainment Stress

[22] By integrating equation (1a) and assuming that the buoyancy varies linearly inside the interface of thickness d_i, *Umlauf and Arneborg* [2009b] express the interfacial transverse transport, q_i, in nondimensional form as

$$\frac{q_i}{Ud_i} \approx -E_k\left(\frac{1}{2} - \frac{r_E}{r_d}\right), \tag{3}$$

where U is the vertically integrated streamwise plume velocity, E_k is the Ekman number, $r_E = E/(C_d + E)$ is the ratio of the entrainment stress to the total down-channel stress, and $r_d = d_i/d$ is the ratio of thickness of the interface, d_i, to the overflow thickness, d. E is the entrainment parameter and C_d is the drag coefficient for a quadratic bottom friction law. According to equation (3) q_i has a geostrophically balanced contribution and an oppositely directed contribution due to entrainment. The transverse transport obeys a purely geostrophic balance if $r_E/r_d \ll 1$. For thick interfaces $r_d = O(1)$ and the requirement is that the entrainment has to be weak compared to bottom friction ($r_E \ll 1$). Applying the drag coefficient, $C_d = 3.7 \times 10^{-3}$, and the entrainment parameter, E, in the range of $3.8 \times 10^{-5} - 3.3 \times 10^{-4}$ calculated from dissipation measurements [*Fer et al.*, 2010b], a conservative estimate for the ratio of entrainment stress to total stress is $r_E = 0.01$–0.08. Thus, according to the CTD/LADCP measurements, the Ekman transport due to entrainment has a negligible effect on the total transport and the transverse interfacial transport is in geostrophic balance. This finding corroborates our conclusions from the mooring data. In our observations, the geostrophically balanced component explains 80% of the variability in the measured transverse velocity. The streamwise momentum budget is dominated by a balance between the pressure gradient and bottom friction, whereas the transverse momentum budget is in geostrophic balance.

[23] The analysis above relies on various assumptions; the relative importance of bottom stress, τ_b, and the interfacial stress, τ_i, can be inferred directly from our cruise data. The survey-averaged values are reported by *Fer et al.* [2010b]. τ_b is obtained from LADCP velocity profiles using law of the wall, and τ_i is estimated using the dissipation rate measurements and LADCP-derived mean shear across the interface, assuming a balance between the shear production, dissipation rate and the buoyancy flux. Resulting values of $\tau_b = 2.1 \pm 0.4$ Pa and $\tau_i = 0.05 \pm 0.02$ Pa yield interfacial stress to total stress ratio of $\tau_i/(\tau_b + \tau_i) \sim 0.02$, in support of the above conclusion. The bottom stress is comparable to that in the Mediterranean outflow plume which varied between 1 to 2.5 Pa [*Johnson et al.*, 1994b, 1994a]. Different than the FBC overflow plume, however, the interfacial stress in the Mediterranean outflow plume was of the same magnitude of the bottom stress in the region of strong entrainment, leading to a total stress of around 5 Pa [*Johnson et al.*, 1994b, 1994a].

[24] To investigate the influence of the time variability on the streamwise stress, we estimate the streamwise, vertically integrated pressure gradient according to

$$P_x = \int_{z_b}^{z_{iso6}} \frac{\partial p}{\partial x}\, dz = \int_{z_b}^{z_{iso6}} \left(\rho_0 \int_{z}^{z_{iso6}} \frac{\partial b}{\partial x}\, d\tilde{z}\right) dz. \tag{4}$$

The streamwise pressure gradient inferred from a pair of moorings separated by about 40 km is approximative and bears uncertainties due to e.g., possible meandering of the plume and that it is not necessarily the same streamline that passes through the two moorings. With this caveat in mind, we infer the following. The pressure gradient varies with the inherent 3–4 day mesoscale oscillations (Figure 9). On the average $P_x = 2.8$ Pa and the pressure gradient is nearly balanced by the survey-averaged bottom stress $\tau_b = 2.1 \pm 0.4$ Pa [*Fer et al.*, 2010b]. In the mean, steady state, i.e., the imbalance is not used for accelerating the flow, the entrainment stress is thus of negligible importance. The streamwise velocity component is correlated with the streamwise pressure gradient (correlation coefficient, $r^2 = 0.8$, also see Figures 6c and 9). In a friction-balanced plume streamwise velocity squared divided by plume thickness is proportional to P_x. Using the height above bottom of the 6°C isotherm as a proxy for plume thickness suggests a relation with $r^2 = 0.58$.

3.4. Role in Mixing

[25] In the vicinity of each of the two moorings, CM and EM, two VMP time series stations were occupied during the 2008 survey. The secondary circulation structure is clearly visible in the average velocity profiles (Figure 10b). Time series are too short to capture the mesoscale variation, but the contrast in profiles illustrates the strong influence of the streamwise flow on the transverse circulation. While the EM station experiences high streamwise velocity (Figure 10b) as the overflow thins (Figure 10a) subsequent of a maximum in

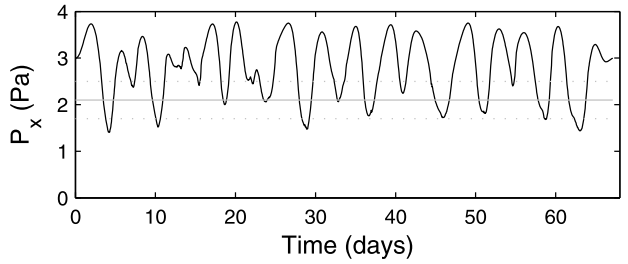

Figure 9. Vertically integrated streamwise pressure gradient, P_x, calculated according to equation (4), between moorings CM and EM. Horizontal grey lines show the survey-averaged bottom stress τ_b (solid) with uncertainty (dashed) inferred from the May 2008 cruise.

plume thickness, the CM station shows lower velocities as the plume thickens. The evolution in plume thickness and the flow strength are also confirmed with the mooring time series (not shown). The high streamwise velocity is associated with enhanced transverse circulation, particularly in the interface layer.

[26] The average gradient Richardson number may be expressed as $\mathrm{Ri} = N^2/S^2$ where $N^2 = -g/\rho\ (\mathrm{d}\rho/\mathrm{d}z)$ is the buoyancy frequency squared, and $S^2 = u_z^2 + v_z^2$ is the shear squared. We calculate Ri at 4 m vertical separation from CTD/LADCP profiles (Ri_{4m}). In order to reduce the contamination by noise at high vertical wave numbers (section 4.3), we low-pass filter LADCP velocity profiles using a 4th order Butterworth filter with 20 m cutoff. To be consistent with velocity profiles, 1 m vertical resolution density profiles are first sorted to remove overturns, and then averaged in 4 m vertical bins and low-pass filtered identical to the velocity profiles. Vertical gradients of velocity and density are obtained by first differencing of the station mean profiles. The profiles of Ri_{4m} (Figure 10c) and the dissipation rate (Figure 10d) from the VMP measurements show that dissipation level increases at EM where Ri_{4m} is less than unity and frequently less than 0.25, the threshold when shear instabilities occur in stratified flows. There is strong shear in the stratified IL at both stations. At EM, the sheared transverse jet in the IL further reduces Ri_{4m}, favoring shear-induced mixing and large dissipation rates in the IL. Average Ri_{4m} between 70 and 160 m HAB at EM (the range in IL where the shear is strong both in u and v) is 0.4. When calculated using the shear from the streamwise component of the velocity alone ($S^2 = u_z^2$), average Ri_{4m} increases to 0.7, by about 75%. The secondary circulation enhances the shear and contributes to reducing Ri. This conclusion supports the numerical modeling results of *Umlauf et al.* [2010, Figure 12] where the cross-channel jet in a gravity current with $E_k = \mathrm{O}(1)$ lowers Ri and provides substantial contribution to the total interfacial shear production.

[27] In addition to enhancing shear-induced mixing, the secondary circulation favors convective mixing in the upslope edge of the plume. Approximately 10 km upslope from CM, at 686 m water depth, an additional mooring sampled temperature at 1 min intervals at 8 levels between 25 and 110 m HAB. Using the temperature difference between the uppermost and bottommost sensors (ΔT) we identify periods of well-mixed layers ($|\Delta T| < 0.01$ K) and convective conditions ($\Delta T < -0.01$ K). The Sea-Bird temperature sensors are accurate to within 2 mK, and in FBC,

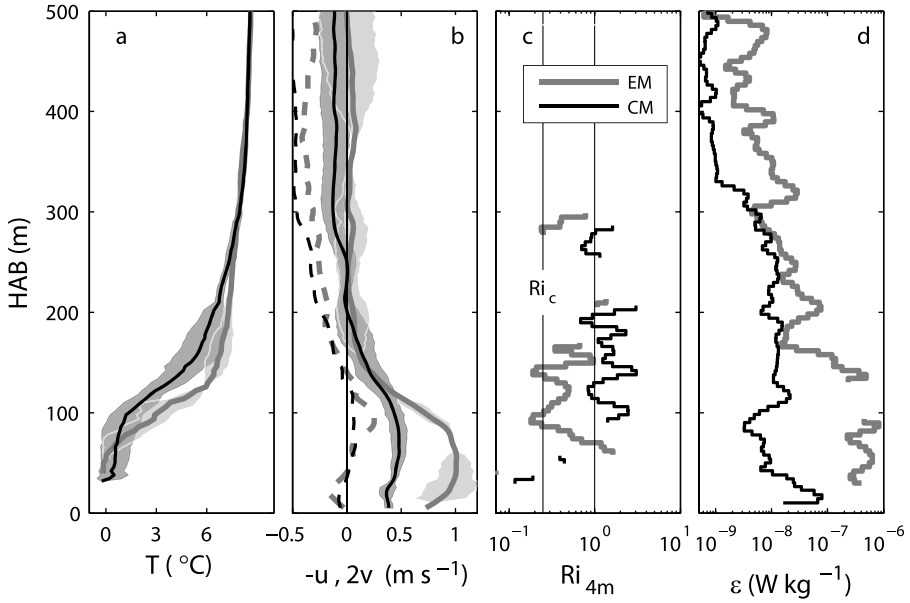

Figure 10. Average profiles of (a) temperature, (b) streamwise ($-u$) and transverse (v, dashed, multiplied by two for clarity) components of the velocity, (c) 4 m gradient Richardson number, and (d) the dissipation rate, ε, collected at the EM (black) and CM (grey) time series stations. All casts are averaged with respect to height above bottom (HAB) in 4 m vertical bins. Shading in T and $-u$ profiles is ± standard deviation. Ri calculations are only shown when measured buoyancy frequency and velocity are greater than imposed error thresholds of 0.5 cph and 1 cm s^{-1}, respectively. Vertical lines in Figure 10c mark the critical $\mathrm{Ri}_c = 0.25$, and Ri = 1.

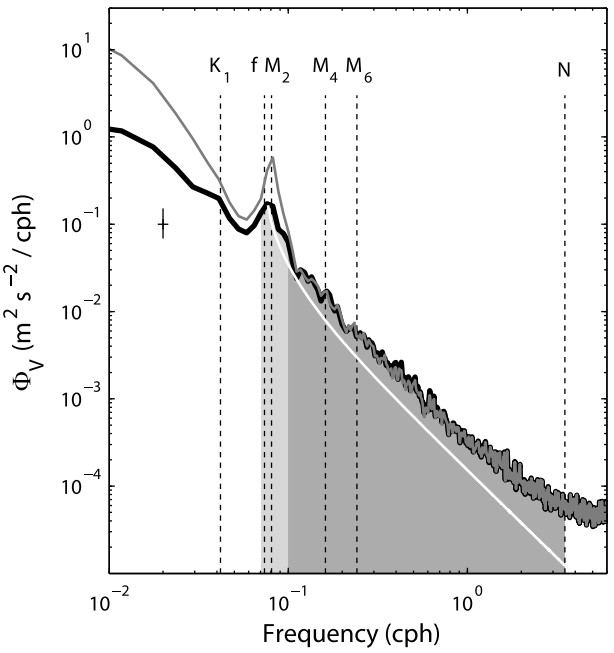

Figure 11. Horizontal total velocity spectra ($\Phi_V = \Phi_u + \Phi_v$), averaged over the layer between the 3°C and 6°C isotherms, calculated from the ADCP data at CM. The spectra are shown for the measured velocity (grey) and for the baroclinic velocity where depth average is removed at each time (black). The GM velocity spectrum with a −2 slope is included for reference (white). The pale and dark grey shaded areas depict the frequency bands used for estimating the kinetic energy. Error bar shows the 95% confidence interval.

temperature is representative of the density to within an r.m.s. error of 0.01 kg m^{-3}. Well-mixed and convective conditions on the slope correspond to periods when the transverse velocity in IL is directed upslope (positive), suggesting a link between transverse circulation and vertical mixing on the upper part of the slope. In total 39 periods were detected with a total duration of 7.3 day when the deepest 110 m on the slope was well mixed in temperature. This corresponds to 9% of the total record length of 63.8 day. While 8 of these periods were of duration longer than 10 h (14 ± 4 h), the remaining lasted for 2 ± 1.8 h. For the mixed conditions, depth average temperature was less than 1.5°C at all times and was colder than zero for 54% of the total duration. During the well-mixed periods 42 convective events were detected, with 6 lasting longer than 4 h (6.3 ± 2.9 h), however, typical duration of the convective events were about 2 h. The mean separation between the convective periods was approximately 3.5 day, correlating with the mesoscale variability.

4. Internal Waves

4.1. Wave Energy in the Interfacial Layer

[28] Internal waves can exist in the thick, stratified IL and can contribute to the mixing of the FBC overflow. In Figure 11, the spectral distribution of the mean total baroclinic velocity of the layer between the 3 and 6°C isotherms is shown at CM, inferred from the ADCP. This instrument, installed in a spherical buoy, experienced tilt less than 5° from vertical at all times, returning high-quality data. The baroclinic velocities are approximated by removing the vertically averaged velocity measured at all levels. The mean spectra of total velocity (i.e. spectrum of twice the HKE density) are then formed by averaging the spectra from all ADCP bins within the 3–6°C layer. This range is well resolved by the ADCP but is only about half the total extent of IL (see Figure 2). Spectra are computed for the north and east component of the measured velocity and the baroclinic velocity. 2048 point (7.1 day) half-overlapping Hanning segments are used giving 18 degrees of freedom. The total spectrum is then formed by adding the two components, $\Phi_V = \Phi_u + \Phi_v$. Internal ADCP bin averaging uses triangular windows with twice the bin size, hence only every other bin is truly independent. The average spectrum in the layer (18 ADCP levels, 9 independent) has then 162 degrees of freedom for the calculation of the 95% confidence interval. Horizontal velocity spectra of the measured velocity and the baroclinic velocity are shown in Figure 11. At frequencies higher than the semidiurnal band, both spectra are identical within 95% confidence. Removing the depth average from the velocity profiles essentially removes the semidiurnal band surface tides and lower frequency variance. The average spectrum at EM is also calculated, however, the ADCP installed in an in-line frame experienced significant tilt >15° for 60% of the record. The average spectrum at EM (not shown) calculated using the portion of the time series when both pitch and roll <15° is similar, both in magnitude and in shape, to that of CM. For reference, the Garrett-Munk (GM) [*Garrett and Munk*, 1972] internal wave spectrum is also shown in Figure 11, calculated using the local f and N. For all frequencies above the semidiurnal frequency the velocity variance distribution at both moorings is more energetic than the GM internal wave spectrum and decreases with frequency at a fairly constant rate in agreement with the GM slope. As the buoyancy frequency is approached, both spectra flatten to white noise.

[29] In the present study, the ADCPs have four beams in Janus configuration with 20° angle from the vertical. Horizontal beam separation increases with increasing vertical distance from the transducers. This beam spreading affects velocity estimates and the frequency spectrum. According to *Lu and Lueck* [1999], see also the appendix of *Peters et al.* [2007], ADCP velocity estimates are not affected by beam spreading when averaged over a time corresponding to 55 beam spreading widths of advection in water. In our case, for a maximum vertical range of 80 m, the horizontal separation is about 58 m. Using a mean advection speed of 1 m s^{-1}, this corresponds to a frequency of 1.1 cycles per hour (cph, 1 cph = $(2\pi/3600)$ s^{-1}), hence beam spreading does not have significant effect in the frequency band of interest.

[30] Based on the current measurements from both RDI-ADCP and RCM7, the kinetic energy associated with the two selected frequency bands, the "near-inertial/semidiurnal" band and the "internal wave" band (marked in Figure 11), is calculated by integrating the total baroclinic velocity spectra over the corresponding band. A vertical profile of the baroclinic kinetic energy for the CM mooring is presented in Figure 12. The upper part of the interfacial layer (150–190 m,

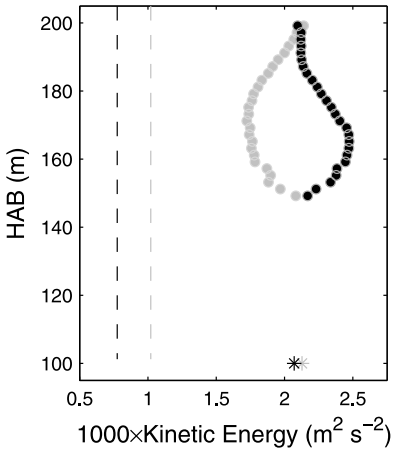

Figure 12. Kinetic energy calculated by integrating the horizontal baroclinic energy spectra from the CM mooring over the near-inertial/semidiurnal band (grey) and the higher frequency internal wave band (black) (see Figure 11). Dots are from ADCP data while the stars are data from the RCM at 100 m HAB. The dashed lines are the corresponding kinetic energy of the GM spectrum, using local f and N, integrated over the near-inertial/semidiurnal band (grey) and the higher frequency internal wave band (black).

see Figure 5b) clearly stands out as highly energetic in the internal wave frequency band, both with respect to the corresponding GM energy and relative to that in the near-inertial band. The mechanisms by which the internal wave energy is elevated in IL are beyond the scope of this paper and merit further studies.

4.2. Influence of Mooring Motion

[31] The total velocity spectra and the inferred energy levels are expected to be influenced by the mooring motion in response to the mesoscale oscillations. Using spectra from three independent data sets at CM, we estimate the spectral signature and energy level associated with the mooring motion. The measurements used are the pressure and temperature recorded by the Microcat at 150 m HAB and the vertical velocity from the 2 m thick ADCP bin centered at 150 m HAB. In Figure 13a the vertical displacement spectra, Φ_ζ, are shown for the displacement, ζ, calculated from the pressure measurement and from the temperature measurement using the mean vertical temperature gradient (from the mean T profile shown in Figure 5). At the level where the spectra are calculated, the mean temperature gradient is $dT/dz = 4.4 \times 10^{-2}$°C m^{-1} and the buoyancy frequency is $N = 3.2$ cph. The variance of the T-derived vertical displacement is significantly larger compared to the actual mooring displacement (from pressure) for all frequencies. We conclude that despite occasional significant motion of the mooring the isotherm displacement spectra are not corrupted.

[32] Another independent comparison is the spectrum of the vertical velocity, Φ_w, measured by the RDI-ADCP and that inferred from the vertical displacement recorded by the Microcat pressure sensor (Figure 13b). Supporting the conclusion from the isotherm vertical displacement spectrum, the variance of the vertical velocity is significantly larger compared to the vertical velocity spectrum associated with mooring motion, estimated from pressure. Φ_w can also be used to infer the vertical displacement spectrum (not shown) as $\Phi_\zeta = \Phi_w/(2\pi\omega/3600)^2$, where the frequency ω is in cph. Integrating Φ_ζ between f and N and taking the square root yields r.m.s. vertical displacements of 43, 15 and 2 m inferred from w, T, and P measurements, respectively.

[33] Following *Levine et al.* [1997], error in displacement variance due to mooring motion can be quantified as $e = \langle d'^2 \rangle + [T_{err}/\langle dT/dz \rangle]^2$ where T_{err} is a typical temperature measurement error (here conservatively set to 0.01°C). A signal-to-noise ratio, SNR, defined as the displacement variance inferred from T divided by e, using 12 hour high-passed data, calculated over 3 h segments, show that 6% of the data has SNR < 5, and on average SNR is about 250.

4.3. Wave Energy Dissipation in the Ambient

[34] We hypothesize that a dominant mechanism for dissipating turbulent energy in the stratified ambient, above the overflow plume, is internal wave breaking. In a slowly varying broadband internal wavefield, the rate of energy dissipation due to wave breaking approximately equals the net energy transfer toward smaller scales [e.g., *Henyey et al.*, 1986; *Gregg*, 1989]. Using vertical profiles of velocity and density resolved at fine scales (order of meters), the viscous dissipation rate of TKE (ε) can be inferred. In essence this is done by comparing and scaling the observed levels of shear and strain, the vertical derivative of isopycnal displacements ζ_z, to the GM levels. The most recent form of the fine-scale parameterization can be expressed as [*Gregg et al.*, 2003]

$$\varepsilon_{IW} = \varepsilon_0 \left(\frac{N}{N_0}\right)^2 \left(\frac{0.1}{k_c}\right)^2 \left(\frac{1+1/R_\omega}{4/3}\right) \left(\frac{2}{R_\omega - 1}\right)^{1/2} L(f,N), \quad (5)$$

where $\varepsilon_0 = 6.7 \times 10^{-10}$ W kg^{-1} is the background dissipation level for GM conditions, and L contains the latitude dependence:

$$L(f,N) = \frac{f \,\mathrm{arccosh}(N/f)}{f_{30}\,\mathrm{arccosh}(N_0/f_{30})}.$$

N is the local buoyancy frequency, f is the local inertial frequency, $N_0 = 5.2 \times 10^{-3}$ s^{-1} (≡3 cph) is the reference stratification and f_{30} is the inertial frequency at 30° latitude. In equation (5), the term with R_ω corrects for the variation in the ratio of N-normalized shear variance to strain variance (shear-strain ratio)

$$R_\omega = \frac{\langle V_z^2 \rangle}{N^2 \langle \zeta_z^2 \rangle}.$$

Here and in the following the variance of x is denoted by $\langle x^2 \rangle$. For the GM model $R_\omega = 3$, $N = N_0$, $f = f_{30}$ and $k_c = 0.1$ cpm, and all correction and scaling terms cancel out leading to $\varepsilon = \varepsilon_0$, i.e., very weak dissipation. The significant figure in ε_0 is not representative of the accuracy of this parameterization, which is approximately a factor of two. The cutoff vertical wave number, k_c, is the wave number up to which the integrated shear variance is approximately $0.7N^2$. Consequently, the ratio of average observed and GM spectral levels at wave numbers less than k_c is $0.1/k_c$. The higher this elevation above GM the higher the dissipation.

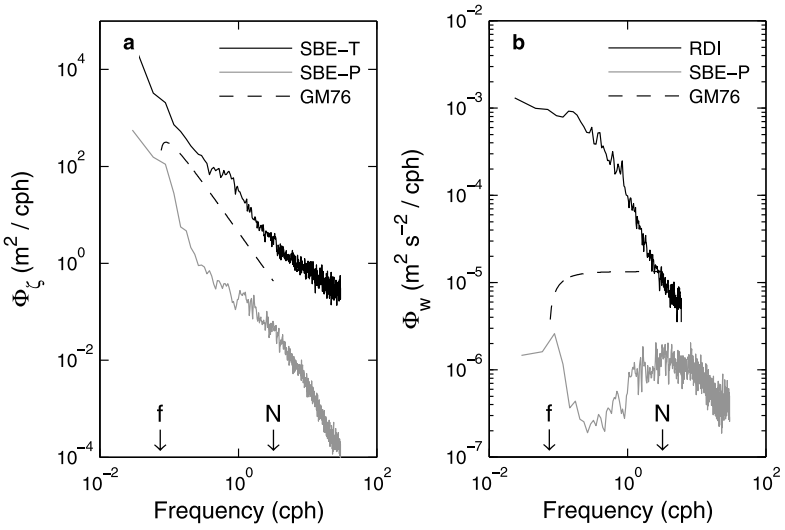

Figure 13. CM mooring (a) vertical displacement spectra calculated from temperature (black) using the mean vertical temperature gradient, and from pressure measurement (grey), (b) vertical velocity spectrum measured by RDI-ADCP (black) and inferred from pressure (grey). All measurements are approximately at the same level (about 150 m HAB). The dashed lines are the GM displacement and vertical velocity spectra using local f and N.

[35] At the repeat stations colocated with EM and CM, in addition to the microstructure profiles, we collected 2 and 4, respectively, CTD/LADCP casts. The two casts at EM were taken only 6 h apart and did not resolve the semidiurnal cycle, whereas the station duration at CM was about 15 h. Above the plume and below the upper 100 m (in the ambient and below the surface layer), we calculate the vertical wave number (k_z) shear spectra from LADCP and strain spectra from CTD profiles between 100 and 610 m depth (i.e. 128 data points for 4 m sampled LADCP and 512 data points for 1 m sampled CTD). We obtain spectra of shear $\Phi_{shear} = (2\pi k_z)^2\, \Phi_V$, and strain $\Phi_{strain} = (2\pi k_z)^2\, \Phi_\zeta$, from the spectra of total velocity (Φ_V) and vertical displacement (Φ_ζ) calculated as averages over half-overlapping 64 and 256 point (256 m) long segments. This gives 12 and 24 degrees of freedom, respectively, for EM and CM. Vertical displacement profiles are calculated relative to the station mean density profile. The shear spectra are normalized by the average N^2 in the corresponding segment. Resulting spectra are shown in Figure 14 together with the GM spectra. The GM spectra are white (constant with k_z) and decay with -1 slope after k_c = 0.1 cpm. This roll-off moves to lower wave numbers as the energy increases [*Polzin et al.*, 1995], shown for the observed shear level by the dashed lines in Figure 14. The average shear spectra from both stations are consistent with the roll-off until the instrumental noise begins to contaminate the spectra at about $1/k_z$ = 50 m. All spectra suggest whitening at low wave numbers. While the shape of shear and strain spectra are consistent at EM, the strain spectrum at CM is white out to higher wave number compared to the shear spectrum.

[36] In application of equation (5) we infer k_c as the first wave number where the integrated N -normalized shear spectrum reaches 0.7. For both stations, this is reached at k_z = 0.0078 cpm, corresponding to a wavelength of 128 m. Variance of shear and strain are then calculated by integrating the corresponding spectrum to k_c, to obtain R_ω. At EM, shear and strain are comparable (R_ω = 1.7), whereas at CM shear is significantly more energetic (R_ω = 6.9). Note, however, EM sampling is of 6 hour duration and is biased. Because the variances are obtained by integrating to 128 m wavelength, the noise contamination is negligible. Fine-scale parameterization leads to dissipation rates of 2.8 × 10^{-8} W kg^{-1} and 5.4 × 10^{-9} W kg^{-1} for EM and CM, respectively. Dissipation rate measured by the microstructure profiler, averaged in the same depth range, is 4.4 × 10^{-9} W kg^{-1} and 2.4 × 10^{-9} W kg^{-1}, with 95% confidence limits of the maximum likelihood estimator from a lognormal distribution [4. 4.8] × 10^{-9} W kg^{-1} [2.3 2.6] × 10^{-9} W kg^{-1}. The agreement between the observed dissipation and that inferred from equation (5) is within 50% at CM. At EM, on the other hand, ε_{IW} is about 6 times the observed value. This can partly be attributed to the lack of sampling throughout the semidiurnal cycle. Furthermore N-normalized shear variance can be dominated by noise in weak stratification [*Kunze et al.*, 2006; *Fer et al.*, 2010a]. At EM the mean stratification is weak with N = 0.0012 s^{-1} (0.69 cph), close to noise level. At CM, $N \sim$ 1.2 cph.

[37] The fine-scale parameterization assumes that energy is transferred from large to small scales through nonlinear wave-wave interactions. In the ambient above the plume this assumption might hold, but will fail near the sloping bottom boundary layer where other processes dominate the scale transformation [*Polzin*, 2004], close to internal wave generation sites, and for internal hydraulic phenomena such as internal hydraulic jumps and direct breaking of internal tides.

4.4. Wave Energy Dissipation in the Interfacial Layer

[38] The energy transfer through the wave spectrum spectral domain in IL can be dominated by different processes due to non-GM shear (e.g. entrainment and mixing at

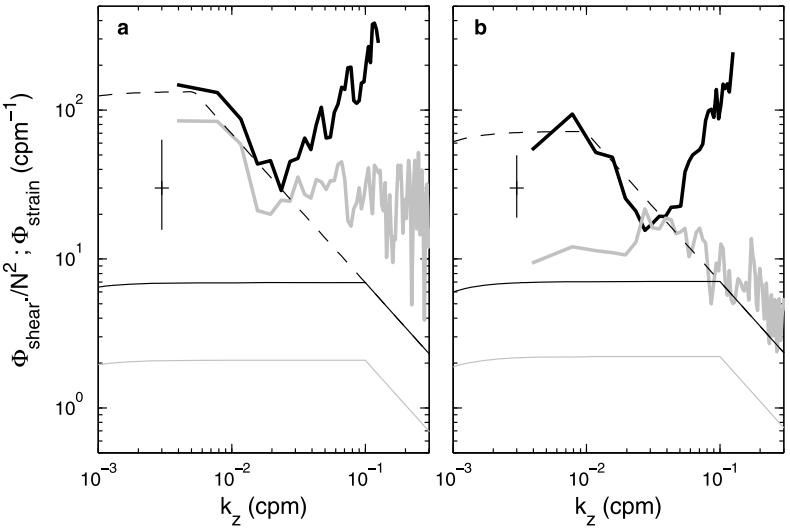

Figure 14. Spectra of shear (black) and strain (grey) obtained from the spectra of total velocity and vertical displacement respectively, using LADCP/CTD data collected during the June 2008 cruise near (a) EM and (b) CM. The canonical GM spectra are shown for reference, together with the GM spectra adjusted to the observed shear level and roll-off extended to k_c. The vertical lines are the 95% confidence intervals, valid for both shear and strain spectra, using 12 (EM) and 24 (CM) degrees of freedom.

the plume-ambient interface, influence of secondary circulation, mesoscale subinertial shear etc.), hence it is ill advised to apply the wave dissipation model of *Henyey et al.* [1986] to the internal wave energy levels measured in IL. Using the present data set, we cannot quantify the relative contribution of internal waves and shear instability to turbulence in IL, nor draw a firm conclusion on the amount of dissipation rate in IL due to internal waves. Internal wave energy levels are elevated relative to GM in the interfacial layer (section 4.1), which, by qualitative analogy to the Gregg-Henyey scaling of dissipation with internal wave energy squared, makes it plausible that internal wave-driven mixing should also be elevated. We conclude that internal wave-induced mixing in IL can be significant and should not be ignored.

5. Concluding Remarks

[39] Observations of hydrography, currents and turbulence from the FBC overflow, conducted in 2008, have been analyzed with emphasis on mixing in the stratified interface, addressing the role of transverse circulation and internal waves. The observations comprise profiles of velocity, hydrography, microstructure temperature and shear, and a 2 month long time series of current, temperature and salinity from moored instruments. Strong temporal and spatial variability characterize the FBC overflow, and the assumption of stationarity is considered to be crude. Similar to the observations of secondary circulation in the FBC near the sill crest [*Johnson and Sanford*, 1992], on the open slope farther downstream secondary circulation exists, however, the dynamics is different: the interfacial Ekman transport is not significant in driving the secondary circulation, but the geostrophically balanced part of the transport in IL plays a key role. Direct turbulence measurements show that the stress due to friction and entrainment at the interface is up to two orders of magnitude less than the stress near the bottom. Transverse flow at the interface is geostrophically balanced with the streamwise pressure gradient. Mesoscale oscillations have a prominent signature in the overflow strength and structure, in general, and affect the transverse circulation, in particular.

[40] The cross-stream flow near the bottom (Ekman transport) and in the interfacial layer (geostrophic transport) effectively contribute to mixing in several ways: by diluting the bottom layer of the plume, by acting as an advective source of buoyancy, by transporting IL water to the right of the streamwise flow, by reducing the Richardson number in IL, and by convection on the upper slope.

[41] The transverse velocity in the interfacial layer deviates slightly from a purely geostrophic flow, but a streamwise pressure gradient nearly balanced by the bottom stress suggests that the overflow is under "frictional control," i.e., nearly geostrophic transverse flow in the interfacial layer opposed by the Ekman transport in the bottom layer. It is noteworthy that despite the small ratio of Ekman layer thickness to plume thickness ($E_k < 1$) of FBC overflow plume, all crucial elements of frictional control are supported by our data.

[42] Above the overflow plume, in the ambient waters, the main mechanism of dissipating turbulent energy is breaking of internal waves, and can be inferred from the fine-scale parameterization of *Gregg et al.* [2003]. In the interfacial layer main mechanism of mixing is the shear instability and entrainment associated with the swift gravity current, enhanced by the secondary circulation. However, we find that the internal wave continuum is energetic in the interfacial layer and may significantly contribute to mixing.

[43] **Acknowledgments.** This work is funded through the Academia agreement between the Norwegian University of Science and Technology and Statoil ASA and by the Research Council of Norway through the

Bipolar Atlantic Thermohaline Circulation (BIAC) project. K.S.S. received partial support from the University of Bergen. We thank Elin Darelius for performing the mooring motion corrections and preparing the mooring data for analysis. We received valuable comments from Lars Umlauf, Lars Arneborg, Hartmut Peters, and two anonymous reviewers.

References

Baringer, M. O., and J. F. Price (1997), Mixing and spreading of the Mediterranean outflow, *J. Phys. Oceanogr.*, *27*, 1654–1677.

Baumert, H. Z., and H. Peters (2009), Turbulence closure: turbulence, waves and the wave-turbulence transition - Part 1: Vanishing mean shear, *Ocean Sci.*, *5*, 47–58.

Borenäs, K. M., and P. A. Lundberg (1988), On the deep-water flow trough the Faroe Bank Channel, *J. Geophys. Res.*, *93*, 1281–1292.

Borenäs, K. M., and P. A. Lundberg (2004), The Faroe Bank Channel deep-water overflow, *Deep Sea Res., Part II*, *51*, 335–350.

Canuto, V. M., Y. Cheng, A. M. Howard, and I. N. Esau (2008), Stably stratified flows: a model with no Ri(cr), *J. Atmos. Sci.*, *65*, 2437–2447.

Darelius, E. (2008), Topographic steering of dense overflows: Laboratory experiments with V-shaped ridges and canyons, *Deep Sea Res., Part I*, *55*, 1021–1034.

Darelius, E., and A. K. Wåhlin (2007), Downward flow of dense water leaning on a submarine ridge, *Deep Sea Res., Part I*, *54*, 1173–1188.

D'Asaro, E. A., and R.-C. Lien (2000), The wave-turbulence transition for stratified flows, *J. Phys. Oceanogr.*, *30*, 1669–1678.

Egbert, G. D., A. F. Bennett, and M. G. G. Foreman (1994), TOPEX/POSEIDON tides estimated using a global inverse model, *J. Geophys. Res.*, *99*, 24,821–24,852.

Ezer, T. (2006), Topographic influence on overflow dynamics: Idealized numerical simulations and the Faroe Bank Channel, *J. Geophys. Res.*, *111*, C02002, doi:10.1029/2005JC003195.

Fer, I., R. Skogseth, and F. Geyer (2010a), Internal waves and mixing in the marginal ice zone near the Yermak Plateau, *J. Phys. Oceanogr.*, *40*, 1613–1630.

Fer, I., G. Voet, K. S. Seim, B. Rudels, and K. Latarius (2010b), Intense mixing of the Faroe Bank Channel overflow, *Geophys. Res. Lett.*, *37*, L02604, doi:10.1029/2009GL041924.

Garrett, C. J., and W. H. Munk (1972), Space-time scales of internal waves, *Geophys. Fluid Dyn.*, *3*(1), 225–264.

Geyer, F., S. Østerhus, B. Hansen, and D. Quadfasel (2006), Observations of highly regular oscillations in the overflow plume downstream of the Faroe Bank Channel, *J. Geophys. Res.*, *111*, C12020, doi:10.1029/2006JC003693.

Girton, J. B., and T. B. Sanford (2003), Descent and modification of the overflow plume in the Denmark Strait, *J. Phys. Oceanogr.*, *33*, 1351–1364.

Gregg, M. C. (1989), Scaling turbulent dissipation in the thermocline, *J. Geophys. Res.*, *94*, 9686–9698.

Gregg, M. C., T. B. Sanford, and D. P. Winkel (2003), Reduced mixing from the breaking of internal waves in equatorial waters, *Nature*, *422*(6931), 513–515.

Hansen, B., and S. Østerhus (2000), North Atlantic-Nordic seas exchanges, *Prog. Oceanogr.*, *45*, 109–208.

Hansen, B., and S. Østerhus (2007), Faroe Bank Channel overflow 1995–2005, *Prog. Oceanogr.*, *75*, 817–856.

Henyey, F. S., J. Wright, and S. M. Flatte (1986), Energy and action flow through an internal wave field: An eikonal approach, *J. Geophys. Res.*, *91*, 8487–8495.

Johnson, G. C., and D. R. Ohlsen (1994), Frictionally modified rotating hydraulic channel exchange and ocean outflows, *J. Phys. Oceanogr.*, *24*, 66–78.

Johnson, G. C., and T. Sanford (1992), Secondary circulation in the Faroe Bank Channel outflow, *J. Phys. Oceanogr.*, *22*, 927–933.

Johnson, G. C., R. G. Lueck, and T. B. Sanford (1994a), Stress on the Mediterranean outflow plume: Part 2. Turbulent dissipation and shear measurements, *J. Phys. Oceanogr.*, *24*, 2084–2092.

Johnson, G. C., T. B. Sanford, and M. O. Baringer (1994b), Stress on the Mediterranean outflow plume: Part 1. Velocity and water property measurements, *J. Phys. Oceanogr.*, *24*, 2072–2083.

Kunze, E., E. Firing, J. M. Hummon, T. K. Chereskin, and A. M. Thurnherr (2006), Global abyssal mixing inferred from lowered ADCP shear and CTD strain profiles, *J. Phys. Oceanogr.*, *36*, 1553–1576.

Levine, M. D., L. Padman, R. D. Muench, and J. H. Morison (1997), Internal waves and tides in the western weddell sea: Observations from ice station weddell, *J. Geophys. Res.*, *102*, 1073–1089.

Lu, Y., and R. G. Lueck (1999), Using a broadband ADCP in a tidal channel. Part I: Mean flow and shear, *J. Atmos. Oceanic Technol.*, *16*(11), 1556–1567.

Mauritzen, C., J. Price, T. Sanford, and D. Torres (2005), Circulation and mixing in the Faroese Channels, *Deep Sea Res., Part I*, *52*, 883–913.

Peters, H., and W. E. Johns (2005), Mixing and entrainment in the Red Sea outflow plume. Part II: Turbulence characteristics, *J. Phys. Oceanogr.*, *35*, 584–600.

Peters, H., C. M. Lee, M. Orlić, and C. E. Dorman (2007), Turbulence in the wintertime northern Adriatic Sea under strong atmospheric forcing, *J. Geophys. Res.*, *112*, C03S09, doi:10.1029/2006JC003634.

Polzin, K. (2004), A heuristic description of internal wave dynamics, *J. Phys. Oceanogr.*, *34*, 214–230.

Polzin, K. L., J. M. Toole, and R. W. Schmitt (1995), Finescale parameterizations of turbulent dissipation, *J. Phys. Oceanogr.*, *25*, 306–328.

Price, J. F., M. O. Barringer, R. G. Lueck, G. C. Johnson, I. Ambar, G. Parrilla, A. Cantos, M. A. Kennelly, and T. B. Sanford (1993), Mediterranean outflow and mixing dynamics, *Science*, *259*, 1277–1282.

Riemenschneider, U., and S. Legg (2007), Regional simulations of the Faroe Bank Channel overflow in a level model, *Ocean Model.*, *17*, 93–122.

Saunders, P. M. (1990), Cold outflow from the Faroe Bank Channel, *J. Phys. Oceanogr.*, *1*, 29–43.

Saunders, P. M. (2001), The dense northern overflows, in *Ocean Circulation and Climate*, edited by G. Siedler et al., pp. 401–417, Academic, Sand Diego, Calif.

Seim, K. S., I. Fer, and J. Berntsen (2010), Regional simulations of the Faroe Bank Channel overflow using a σ-coordinate ocean model, *Ocean Model.*, *35*, 31–44, doi:10.1016/j.ocemod.2010.06.002.

Stahr, F. R., and T. B. Sanford (1999), Transport and bottom boundary layer observations of the North Atlantic Deep Western Boundary Current at the Blake Outer Ridge, *Deep Sea Res., Part II*, *46*, 205–243.

Umlauf, L. (2009), The description of mixing in stratified layers without shear in large-scale ocean models, *J. Phys. Oceanogr.*, *39*, 3032–3039.

Umlauf, L., and L. Arneborg (2009a), Dynamics of rotating shallow gravity currents passing through a channel. Part I: Observation of transverse structure, *J. Phys. Oceanogr.*, *39*, 2385–2401.

Umlauf, L., and L. Arneborg (2009b), Dynamics of rotating shallow gravity currents passing through a channel. Part II: Analysis, *J. Phys. Oceanogr.*, *39*, 2402–2416.

Umlauf, L., L. Arneborg, R. Hofmeister, and H. Burchard (2010), Entrainment in shallow rotating gravity currents: A modeling study, *J. Phys. Oceanogr.*, *40*, 1819–1834.

Visbeck, M. (2002), Deep velocity profiling using lowered acoustic Doppler current profilers: Bottom track and inverse solutions, *J. Atmos. Oceanic Technol.*, *19*, 794–807.

Wåhlin, A. K. (2002), Topographic steering of dense currents with application to submarine canyons, *Deep Sea Res., Part I*, *49*, 305–320.

Wåhlin, A. K. (2004), Downward channeling of dense water in topographic corrugations, *Deep Sea Res., Part I*, *51*, 577–590.

I. Fer, Geophysical Institute, University of Bergen, Allégaten 70, N-5007 Bergen, Norway. (Ilker.Fer@gfi.uib.no)

K. S. Seim, Department of Marine Technology, Norwegian University of Science and Technology, O. Nielsens vei 10, Tyholt, N-7491 Trondheim, Norway.